Shaped Pd—Ni—Pt Core-Sandwich-Shell Nanoparticles: Influence of Ni Sandwich Layers on Catalytic Electrooxidations

Brian T. Sneed,[†] Allison P. Young,[†] Daniel Jalalpoor,[‡] Matthew C. Golden,[†] Shunjia Mao,[†] Ying Jiang,[§] Yong Wang,[§] and Chia-Kuang Tsung[†,*]

[†]Department of Chemistry, Merkert Chemistry Center, Boston College, 2609 Beacon Street, Chestnut Hill, Massachusetts 02467, United States, [‡]Department of Chemistry, Technische Universität Berlin, Strasse des 17. Juni 135, 10623 Berlin, Germany, and [§]Center of Electron Microscopy and State Key Laboratory of Silicon Materials, Department of Materials Science and Engineering, Zhejiang University, Hangzhou 310027, China

ABSTRACT Shape-controlled metal nanoparticles (NPs) interfacing Pt and nonprecious metals (M) are highly active energy conversion electrocatalysts; however, there are still few routes to shaped M—Pt core—shell NPs and fewer studies on the geometric effects of shape and strain on catalysis by such structures. Here, well-defined cubic multilayered Pd—Ni—Pt sandwich NPs are synthesized as a model platform to study the effects of the nonprecious metal below the shaped Pt surface. The combination of shaped Pd substrates and mild reduction conditions directs the Ni and Pt overgrowth in an oriented, layer-by-layer fashion. Exposing a majority of Pt(100) facets, the catalytic performance in formic acid and methanol electro-oxidations (FOR and MOR) is assessed for two different Ni layer thicknesses and two different particle sizes of the ternary sandwich NPs. The strain imparted to the Pt shell layer by the introduction of the Ni sandwich layer (Ni—Pt lattice mismatch of ~11%) results in higher specific initial activities compared to core—shell Pd—Pt bimetallic NPs in alkaline MOR. The trends in activity are the same for FOR and MOR electrocatalysis in acidic electrolyte. However, restructuring in acidic conditions suggests a more complex catalytic behavior from changes in composition. Notably, we also show that cubic quaternary Au—Pd—Ni—Pt multishelled NPs, and Pd—Ni—Pt nanooctahedra can be generated by the method, the latter of which hold promise as potentially highly active oxygen reduction catalysts.

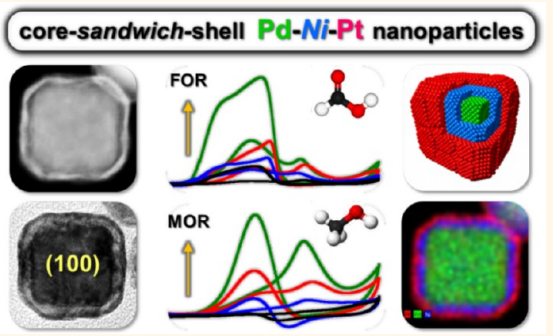

KEYWORDS: Pd · Ni · Pt · nanoparticle synthesis · lattice strain · electrocatalysis · core—shell · multilayered · shape · sandwich

There has been a growing interest in the preparation of shaped binary and ternary metal nanoparticles (NPs) comprising nonprecious metals (M) as they achieve better activity, stability, and efficiency as electrocatalysts for energy conversion chemistry.[1−9] In particular, such shaped M—Pt NP oxygen reduction electrocatalysts could advance the commercial viability of automotive hydrogen fuel cells.[10] The superior performance of shaped M—Pt NPs merits their study, but the many factors that influence catalytic behavior in these complex systems (ligand, ensemble, geometric, and strain effects) are difficult to parse out.[11] Often it remains that the most active and stable structures for these catalysts are composed of layers of Pt atoms above an M—Pt core, and so the target structure is re-envisioned as a core—shell NP architecture.[10,12] In addition, it is shown that thin M-sandwich layers can exist due to restructuring during the reactions,[13] and indeed there is experimental and theoretical work which discusses the stability of various Pt—M—Pt sandwich and multilayered Pt-skin structures.[12,14−16] The aforementioned M—Pt NP surfaces reconstruct to the Pt-skin motif due to dealloying (leaching) of the nonprecious component from the surface during potential cycling in acidic conditions.[17,18] Recent work predicts M—Pt NPs comprising a Pd—Ni core and Pt-shell to be more stable and highly active electrocatalysts for oxygen reduction.[12] All of this information suggests the investigation of core—shell and multishelled M-Pt nanoarchitectures to be a promising direction for fundamental catalysis research.

Despite the advancement of M—Pt NP electrocatalysts, such as Ni, there are few

* Address correspondence to frank.tsung@bc.edu.

Received for review April 24, 2014 and accepted June 4, 2014.

Published online June 04, 2014
10.1021/nn502259g

established methods for creating core−shell M−Pt NPs with well-defined shape control. Current strategies for producing Ni−Pt alloy NPs with shape control require Ni and Pt ions to be co-reduced.[19] Usually, this is accompanied by a variety of capping/shaping agents.[20−22] Wu *et al.* have recently contributed a shape-controlled synthesis for Ni octahedra,[23] and others have demonstrated control of shape for bimetallic systems with core−shell Pd−Cu and Ag−Ni nanocubes.[24,25] While these works are excellent examples of the power in colloidal synthesis, the synthesis with rational structural control remains a challenge. Also, various cleaning methods are required due to the strong bonding capping agents used in these organic phase syntheses.

An aqueous,[26] layer-by-layer epitaxial overgrowth approach[24,27−32] to shape-controlled M−Pt core−shell NPs would be desirable for the exploration of strained nanoarchitectures, as well as for the opportunity to study strain effects on catalysis by multishelled structures. Direct control of the size, overall shape, and the thickness of each layer in a core-sandwich-shell nanostructure would provide a platform to gain better understanding of lattice strain effects on catalytic activity and perhaps elucidate the limits for these effects experimentally. Previous works show tuning the shell thickness and NP size as a way to increase catalytic activity.[12,33] The activity changes observed with expansive or compressive lattice strain (from the lattice mismatch at metal−metal interfaces) have been attributed to subtle altering of the binding energies of adsorbates, by way of perturbation of the surface d-band.[18,34] The d-band model offers a straightforward design principle to fine-tune Pt-based electrocatalysts,[11] yet there is still much debate over its validity as a general descriptor and predictor of catalytic activity.[35,36]

Herein, we present an aqueous, low temperature route to shape-controlled Pd−Ni−Pt core-sandwich-shell NPs using cetyltrimethylammonium bromide (CTAB) as the capping agent and hydrazine as the reducing agent. Scheme 1 demonstrates how Pd cubes function as shaped crystal substrates which catalyze and direct the oriented overgrowth of Ni. Pt ions are added after the Ni overgrowth to "trap" the metallic Ni phase and complete the layer-by-layer synthesis of the shaped ternary metal NPs. This method allows for control of the overall size, shape, and layer thickness by the choice of substrate and amount of precursor salts added in the growth solution.

The strategy presented here is attractive toward the end-goal of understanding the impact of lattice strain on the catalytic performance of core−shell NPs. The cubic Pd−Ni−Pt structures are investigated as formic acid oxidation (FOR) and methanol oxidation (MOR) electrocatalysts, for which the Pt(100) facets are expected to have higher activity.[37] We discuss the findings of increased specific activity of the catalysts with a

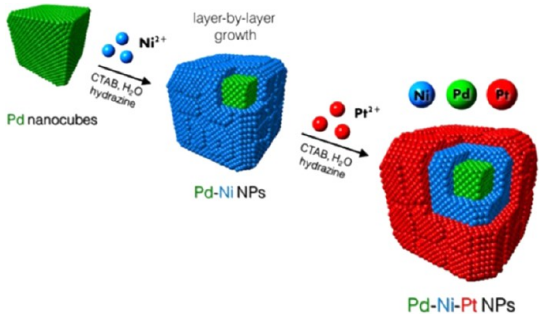

Scheme 1. Synthesis of cubic Pd−Ni−Pt core-sandwich-shell nanoparticles.

Ni-sandwich layer as being due to strain on Pt by the Ni layers beneath the surface. The durability of the different catalysts is assessed, and the smaller trimetallic Pd−Ni−Pt nanoparticles retain the highest activity over time over both the larger ternary NPs and the Pd−Pt control NPs for MOR in alkaline solutions. The trends in activity are similar in acidic conditions; however, because of dealloying and restructuring from potential cycling in acid, their behavior may be more a result of a composition change at the surface, rather than from strain. We further show that an octahedral morphology can be produced by substituting Pd octahedra for the Pd nanocubes in the synthesis. These NPs could be the subject of future studies in oxygen reduction catalysis. Finally, we use the strategy to create quaternary, core-triple-shelled Au−Pd−Ni−Pt NPs with a cubic shape at a size of ∼20 nm. To our knowledge, the novel, shaped multishelled nanoparticles shown here are unprecedented in the literature.

RESULTS AND DISCUSSION

Synthesis of Pd−Ni−Pt Sandwich Nanoparticles. In attempting to synthesize shaped Pd−Ni−Pt multilayered NPs by a wet chemical route, insights were gained from earlier works that successfully demonstrated control of Ni at this size scale. Grzelczak *et al.* were able to produce Ni NPs of different sizes by adjusting the Ni^{2+} to reducing agent ratio in the growth solution and observed size-dependent magnetic properties.[38] Their synthesis was accomplished in water at low temperatures using hydrazine as the reducing agent and CTAB surfactant. The authors confirmed metallic Ni in their work using X-ray structural analysis; however, it was speculated that the surface remained passivated by several oxide layers. Moreover, no control of faceting was reported. This general strategy was utilized to make Ni nanostructures in several of their works,[39−41] while others have since published variations of the Ni-reduction method.[42−44] Recent syntheses yield more complex Ni nanostructures[45,46] and theoretical work proposes and describes the faceting of Ni crystals.[47]

Liz-Marzán's group showed that the Ni NPs could only be formed in this synthesis system under certain conditions: (1) catalytic Pt nanoparticle seeds must be

introduced for the overgrowth of Ni; (2) the growth solution must be sealed to trap the H_2 gas evolved during the synthesis, which promotes Ni reduction and limits surface oxidation; and (3) the growth must occur without magnetic perturbations, such as a stir bar in the growth solution, otherwise the particles may collect and precipitate prematurely, or fuse into chains or wires. We hypothesized that we could make use of this approach, by reducing Ni on shaped Pd substrates instead of small Pt seeds. Their use of mild conditions with ionic surfactants resembled the conditions used for seed-mediated growth[31,48,49] of other metal NPs from our previous work with Au, Pd, and Rh.[27−29,50] It was feasible that combining the strategies would lead to a greater control of Ni faceting in the overgrowth, which has not been attempted before.

In a typical synthesis of Pd−Ni−Pt nanoparticles, shaped Pd substrates (nanocubes) were prepared following procedures in the literature,[27−29] and dispersed into an aqueous solution of CTAB in a small glass vial. Nickel ions were then added in the form of nickel(II)-chloride hexahydrate ($NiCl_2 \cdot 6H_2O$), and an amount of hydrazine monohydrate solution was added last. The vial was sealed and maintained in a water bath at 50 °C for ∼2 h (without stirring) until a color change occurred indicating the Ni overgrowth. Pt ions were then injected in the form of K_2PtCl_4, and heating continued in the water bath for ∼1 h. The ternary metal particles were then removed from heat and collected by centrifugation at 4000 rpm, redispersed, and washed for characterization. In other works, the problem of surface oxidation was avoided by alloying (co-reduction) or by working in organic solvent; however, it is shown that oxides can still form on the surface of such structures in these conditions, especially in aqueous solutions.[24,51] Accordingly, we attempted to prevent oxide formation by "capping" of the Ni layer with overgrowth of Pt in the same "pot". This simultaneously addresses the issue of surface oxidation and creates the desired shaped M-Pt core−shell motif desired for catalysis.

Characterization of Pd−Ni−Pt Sandwich Nanoparticles by TEM. The "trapped" metallic Ni phase in the Pd−Ni−Pt NPs can be observed by contrast in transmission electron microscope (TEM) images shown in Figure 1. Three types of NPs with different sizes and Ni layer thicknesses were synthesized. The NPs in Figure 1a−c were synthesized by introducing 100 and 50 μL of the Ni and Pt precursors, respectively, to growth solutions containing ∼30 nm Pd nanocubes. This resulted in ∼2.5 nm of Ni and 1.6 nm of Pt layers. Particles in Figure 1d−f were synthesized similarly, excepting for a doubling of the amounts of the Ni and Pt metal precursors. This led to 4.1 nm of Ni and 1.6 nm of Pt overgrowth. The NPs shown in Figure 1g−i were created using smaller, ∼12 nm Pd nanocubes in place of the larger substrates, resulting in NPs approximately

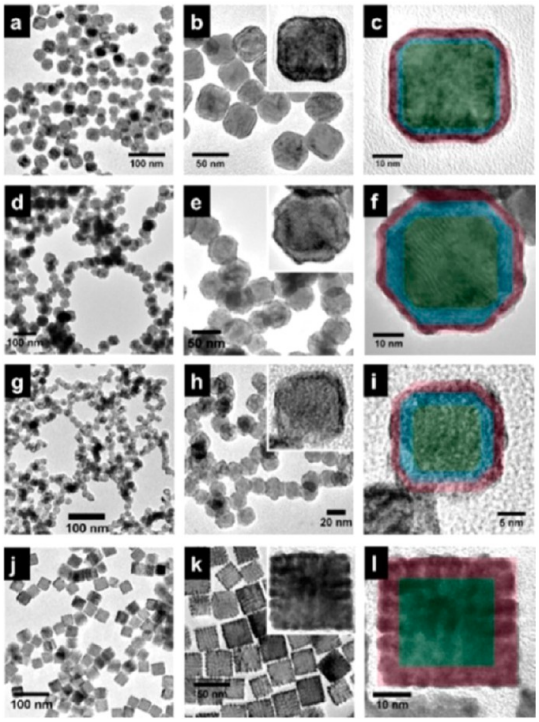

Figure 1. TEM and recolored TEM images of cubic Pd−Ni−Pt and Pd−Pt NPs. (a−c) Pd−Ni−Pt NPs synthesized with ∼2.5 nm Ni sandwich; (d−f) NPs synthesized with ∼4.1 nm Ni sandwich; (g−i) smaller ∼20 nm Pd−Ni−Pt NPs; and (j−l) Pd−Pt core−shell NPs. The original TEM images that were recolored are shown as insets in the upper right of images in the middle column. The Pd, Ni, and Pt regions are shown under green, blue, and red transparencies, respectively, in the recolored images.

∼20 nm in size. Nickel is observed in the TEM images as a lighter phase "sandwiched" between a dark Pd core and a darker Pt surface layer. The difference in contrast is due to the increased electron scattering of the heavier 4d and 5d metals. Recolored TEM images in Figure 1 highlight the different metal phases in the structure. The final truncated cubic morphology is a result of the well-defined cubic shape of the Pd substrates and the layer-by-layer overgrowth. The roughened appearance of the surface is likely due to the lattice mismatch (∼10−11% for these metals) and high degree of strain and defects imparted by having the Ni "sandwiched" between the Pd and Pt layers. Core−shell Pd−Pt NPs also shown in Figure 1j−l lack the Ni layer and are used for comparison as a control in X-ray diffraction and electrochemical catalysis studies presented later in this work; such structures have also shown enhanced performance in the literature as electrocatalysts.[28,52]

Analysis of Structure, Composition, and Strain in Pd−Ni−Pt Sandwich Nanoparticles by STEM/EDX, HAADF, HRTEM Imaging, and XRD. To investigate the composition, conformal overgrowth, and to confirm the core-sandwich-shell structure of the Pd−Ni−Pt NPs, X-ray elemental analysis was carried out. Element maps from scanning transmission electron microscopy with energy

dispersive X-ray spectroscopy (STEM/EDX) and high angle annular dark field images (HAADF) are given for the NPs in Figure 2a–f. There is a clear distinction between the lower mass Ni phase and heavier Pd and Pt phases in the HAADF images in Figure 2a,b as was observed in TEM. Here the Ni appears as a dark band between bright Pt and Pd regions. The STEM/EDX maps for each metal are given in Figure 2c–e with the overlaid map in Figure 2f confirming the double-shelled structure of the Pd–Ni–Pt NPs. The HRTEM image in Figure 2g shows continuous epitaxy from the Pd core through the Ni phase to the Pt shell. The size of the Ni–Pt shells is around ~4 nm, and this is composed by a ~2.5 nm layer of Ni. Measurements of the *d*-spacings in the HRTEM image in Figure 2g agree with the proposed core-sandwich-shell structure in that the (200) *d*-spacing becomes smaller traveling away from the Pd core from ~0.199 to ~0.193 nm in the Ni layer, but then increases near the Pt surface back to ~0.200 nm. This suggests the Pt atoms at the surface experience compression, and we speculate that thicker Ni layers could impart more strain to the Pt surface, by increasing influence of Ni's smaller lattice parameters. We also note that none of the measured *d*-spacings approach the larger bulk NiO (200) *d*-spacing of 0.208 nm, which indicates a metallic Ni layer. This is discussed in more detail following the surface characterization by TEM.

The surface structure was probed by high resolution TEM (HRTEM) for individual particles and orientations shown in Figure 3. The overall truncated cubic morphology is apparent in Figure 3a,b with a model of the double-shelled particles inset of (a). In Figure 3c, square lattice patterns can be observed for NPs lying on the cube face ([100] zone axis). Figure 3d shows the rhombic (distorted hexagonal) lattice images for NPs lying on the cube edge ([110] zone axis). Both sets of images allow for examination of the proposed Pt(100) surface planes and epitaxy through the Ni and Pt shells. From these images and observation of several other NPs we can conclude they are primarily (100)-dominant in faceting, and that the Ni and Pt overgrowth occurs epitaxially, with some "lifted" terraces and steps at the surface, and edge dislocations in the shell produced by defects from the lattice misfit. In a lattice image of the corner of a Pd–Ni–Pt NP on edge in Figure 3e, an approximately ~25° curvature is observed in the atomic planes extending at different angles toward the surface, which we believe is also a result of the highly strained interfaces meeting at the vertex of the cubes. A similar observation of strain in Ni nanostructures has been described by Wang *et al.*[29] They show a nearly ~40° reversible "flip" in the unit cell of Ni nanowires induced by bending of the nanostructure.

The questions of oxide content and strain within the Ni phase are addressed by analysis of powder X-ray diffraction (XRD) of the Pd–Ni–Pt NPs and this is shown in Figure 4a,b. It is first noted that no diffraction

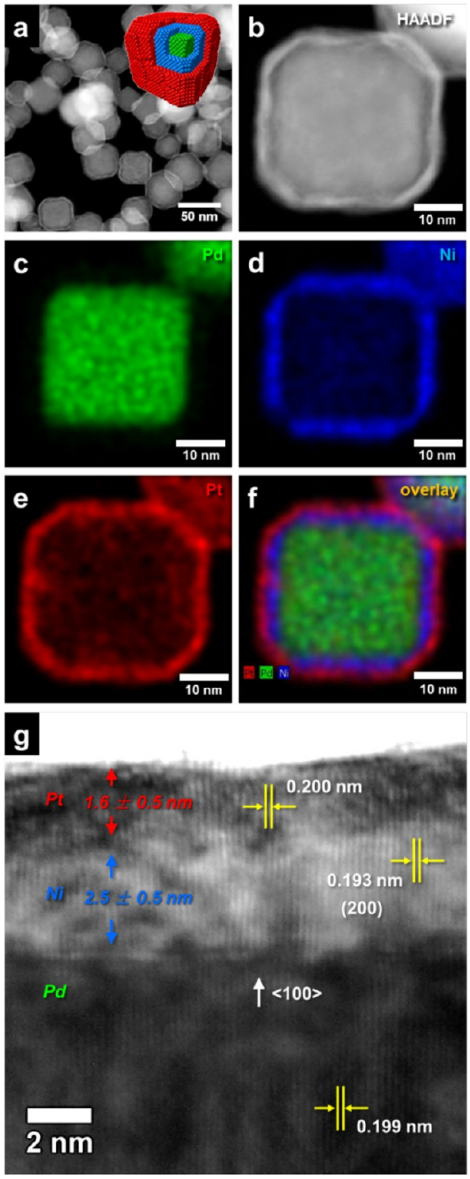

Figure 2. HAADF images, STEM/EDX elemental maps, and an HRTEM image of Pd–Ni–Pt NPs with a ~2.5 nm Ni layer. (a and b) HAADF images; (c–e) STEM/EDX element maps for Pd, Ni, and Pt, respectively, taken for the NP in (b); (f) the image containing the overlaid maps; and (g) HRTEM cross section of a NP showing the layer thickness and measured 200 *d*-spacings. A structural model is given in the inset of (a).

peaks corresponding to the bulk NiO positions can be observed for the samples. The spectrum for NPs with a ~2.5 nm Ni sandwich layer shows a single fcc diffraction pattern similar to the bulk Pd reference. Peaks were observed for the thicker NPs with a ~4.1 nm Ni sandwich layer close to the metallic Ni position. This global information shows that little to no oxide is forming during or after the synthesis and that metallic Ni resides within the sandwich layer. The pattern also suggests that the Ni lattice parameters may come closer to the bulk values with increasing thickness of the Ni sandwich layer (with decreasing influence of core and shell lattices).

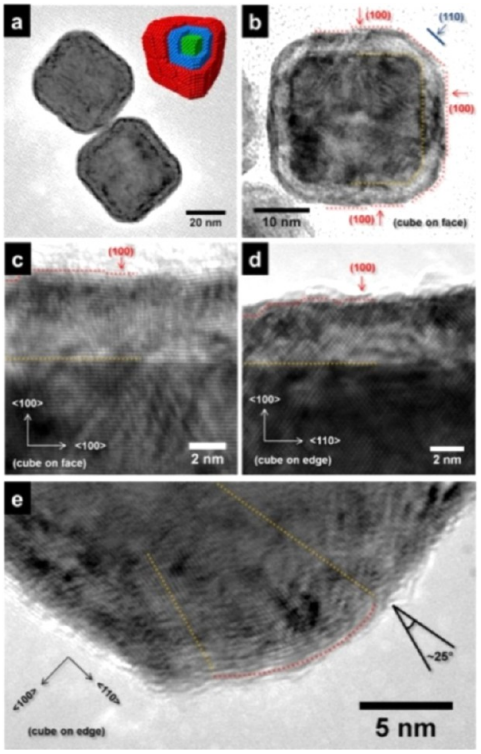

Figure 3. TEM and HRTEM images of Pd−Ni−Pt NPs. (a and b) TEM images showing the truncated cubic morphology with crystal model inset in (a). (c−e) HRTEM lattice images showing the epitaxy and surface structure. For the image in (c), square 2D lattices are obtained from viewing a NP down the 100 axis (cube lying on face), and for (d and e), the lattices come from viewing in the 110 direction (cube lying on edge). The image in (e) shows the lattice distortion in the shell brought about by the high interfacial mismatch for the metal layers (~10−11%) meeting at a corner.

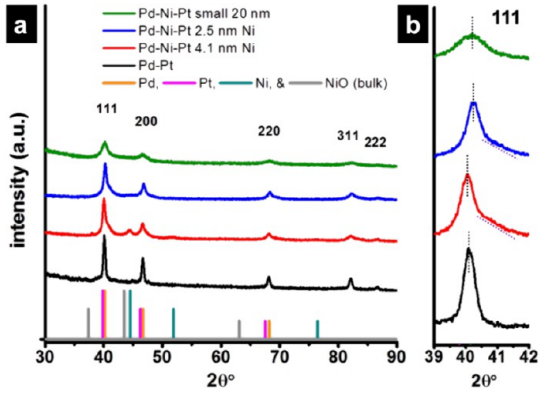

Figure 4. (a) Powder XRD spectra of the different Pd−Ni−Pt and Pd−Pt NPs with peak positions of bulk Pd, Ni, Pt, and NiO for reference. Plot (b) magnifies the 111 region to show the peak shift and tailing of the Pd−Ni−Pt NPs as compared to the Pd−Pt NPs.

XRD data is a good qualitative tool to indicate the existence of lattice strain. Both XRD spectra for the different shell thicknesses of Pd−Ni−Pt have peak "tails" in the direction of higher 2θ degrees. The magnification of the 111 region is displayed in Figure 4b. The tailing is a result of strain in the Ni layer, whereby the Ni lattice expands and Pd and Pt lattices compress. This tailing feature does not appear in the Pd−Pt control, and so corroborates with strain emanating from the introduction of the Ni sandwich layer. There is a lack of the tailing feature in the smaller Pd−Ni−Pt NPs because of the smaller domain size and broadening in the distribution. The maximum peak positions of all of the Pd−Ni−Pt NPs are shifted to the right of the bulk Pd $2\theta°$ and little area under the peaks lie at the bulk Pt diffraction lines, especially for the higher angle 200 and 220 peaks. The exact amount of strain is not straightforward to assess from these shifts because of the differences between the spectra regarding the presence of broadening, the tailing feature, and the appearance of the "Ni" peak in the larger-sized, thicker-shelled NPs.

Electrocatalysis by Pd−Ni−Pt Sandwich Nanoparticles. The catalytic properties of the cubic Pd−Ni−Pt NPs of different sizes and shell thicknesses were studied in the electrooxidation of methanol and formic acid. It is generally believed that both of these catalytic reactions readily occur on more open (100) and (110) surfaces of Pt as opposed to the close-packed (111) facets.[37] Significant improvements have been made to Pd and Pt MOR catalysts by addition of a transition metal to the structure, including alloyed and core−shell structures.[53−58] In our work, different shell thicknesses and sizes of Pd−Ni−Pt NPs are compared alongside the Pd−Pt core−shell NP control. Cyclic voltammetric (CV) and chronoamperometric curves (CA) were obtained for the catalysts of different sizes and Ni thicknesses to show both activity and stability. Typical blank scans in acidic and alkaline electrolyte solutions are shown in Supporting Information Figure S4a,b. Integration of the current collected from the hydrogen desorption peak was used to determine the electrochemical surface area of the different catalysts. This surface area was then used to normalize the catalytic activity for the electrooxidation reactions. The CV plots of initial activity, bar plot summaries, and CA curves for alkaline MOR, and for MOR and FOR in acidic conditions, are shown in Figures 5 and 6, respectively.

FOR and MOR on Pt surfaces proceed by formation of intermediates, which are oxidized and removed on the forward and reverse scans.[37] We use the forward and reverse scan peak current densities to discuss the initial activity of the various catalysts for FOR and MOR in acidic and basic solutions. It has been reasoned that a sandwich layer consisting of a single atomic monolayer of mismatching nonprecious metal would impart little to no strain to a Pt monolayer surface in Pt−M−Pt structures; therefore, any changes in catalytic behavior are predicted to arise primarily through ligand effects.[11] In contrast, for the case of multiple sandwich layers and more than one monolayer of Pt surface atoms (the case here), ligand effects are expected to be minimalized, and the influence of lattice strain is

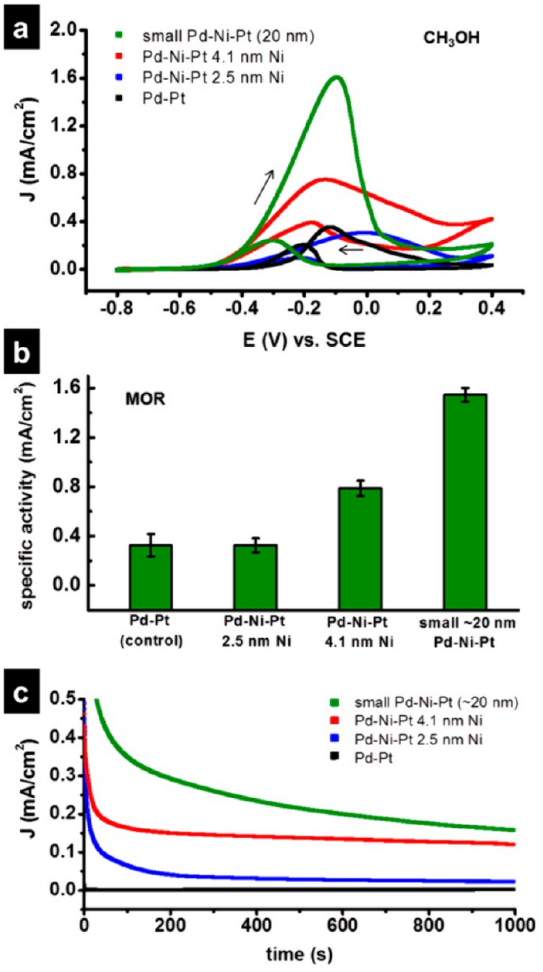

Figure 5. Cyclic voltammetry and chronoamperometry of multilayered Ni nanoparticles showing the catalytic activity for methanol electrooxidation in alkaline conditions. (a) CV cycles obtained in solutions which were 0.1 M in KOH and 0.05 M in CH_3OH, and (b) bar graph of trends in catalyst specific activity showing the average peak current densities for multiple batches of each catalyst. (c) CA curves for the different NP catalysts for MOR at −0.1 V *vs* SCE to show the transient current density.

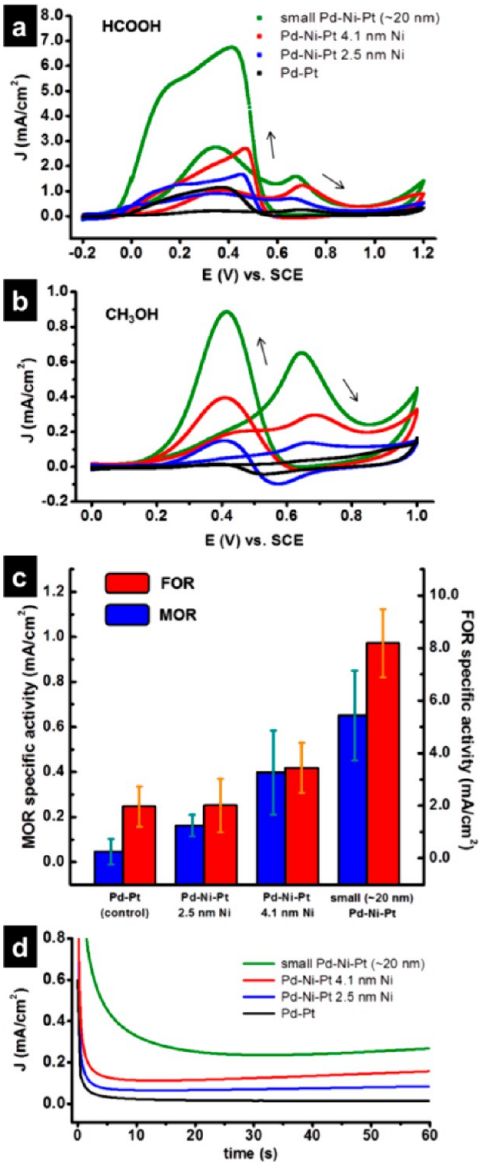

Figure 6. Cyclic voltammetry and chronoamperometry of multilayered Ni nanoparticles showing the catalytic activity for electro-oxidations in acidic conditions. (a) CV cycles obtained in solutions which were 0.5 M in both HCOOH and $HClO_4$, (b) CV curves obtained in solutions which were 0.5 M in both CH_3OH and H_2SO_4, and (c) bar graph of trends in specific activity for each reaction. Multiple batches of each catalyst were synthesized and their peak current densities averaged. (d) CA curves for the different NP catalysts for FOR at 0.4 V *vs* SCE.

expected to be the major contributor to catalysis, assuming restructuring due to dealloying or leaching of the nonprecious component does not occur to a significant extent because of the relatively thick Pt surface layer.[18] As the Ni layer thickness increases for the Pd−Ni−Pt NPs, we would expect the influence of the mismatch to become greater, and so the perturbation to Pt surface atoms may be increased, resulting in changes to catalytic activity.

Electrocatalytic Oxidation of Methanol in Alkaline Electrolyte. To test the hypothesis of a strain influence on catalysis, CV scans were carried out for MOR in alkaline solutions shown in Figure 5a. It was observed that the larger, thicker Ni-layered NPs showed current density at ∼0.8 mA/cm^2. The catalysts with thinner Ni layers and the Pd−Pt control showed similar peak activities around ∼0.4 mA/cm^2, at best, roughly half the activity of the Pd−Ni−Pt NPs with thicker shells. This confirms a diminished strain effect for thin Ni sandwich layers and increasing strain from larger Ni amounts. In addition, the ratio of the forward to reverse scan peak currents is much higher with the sandwich catalysts compared to the control, which shows more efficient oxidation and CO-tolerance for these catalysts.[54,59] A bar plot summary in Figure 5b for MOR in base demonstrates the average activity across different catalyst batches to be consistent. Smaller Pd−Ni−Pt NPs had a much higher current density compared to the other catalysts at ∼1.6 mA/cm^2, showing that the

design could be extended down to size ranges that are more relevant for industrial applications. Figure 5c gives CA curves for MOR in alkaline solution generated by holding the voltage at −0.1 V *vs* SCE. This value was chosen because it overlapped with the position of the forward oxidation peak. These transient current density curves follow similar trends in activity, as for the CV experiments, with the Ni-sandwiched catalysts holding the highest activity over time.

Electrocatalytic Oxidation of Formic Acid and Methanol in Acidic Electrolyte. Improvement of FOR and MOR electrocatalysis in acidic conditions was also observed. For FOR catalysis shown in Figure 6a, it can be seen that the larger Pd−Ni−Pt NPs again outperform the Pd−Pt control. Catalysts with thicker Ni layers show higher current densities (nearly double) compared to the thinner-shelled NPs. The low forward scan peak for each of the catalysts is indicative of the Pt indirect pathway,[37] confirming the surface composition. The smaller sized Pd−Ni−Pt NPs have the highest specific activity at ∼7 mA/cm^2. These trends follow suit in MOR in acidic electrolyte shown in Figure 6b, with the large Pd−Ni−Pt NPs with thicker Ni layers achieving ∼0.4 mA/cm^2. Again the smaller sized Pd−Ni−Pt cubic NPs attained the highest activity at ∼0.8 mA/cm^2. The similar trends in reactivity observed between the different catalytic oxidations could be expected based on the similarity of the reaction pathways on Pt, following direct oxidation to CO_2, and indirect oxidation through adsorbed carbonaceous intermediates, such as CO and formate.[37] In fact, all of the Pd−Ni−Pt ternary metal NP structures outperform the Pd−Pt control. A summary of the specific activities for both reactions in acid electrolyte is given in the bar plot in Figure 6c, where initial activity for different batches of each of the four catalysts were again averaged to show the consistency. We note the higher activity for MOR catalysis in base is generally ascribed to adsorbed hydroxyls assisting in the oxidation reaction.[58]

The CA studies given in Figure 6d show the catalyst durability for FOR at constant 0.4 V; chosen due to the location of the oxidation peak. The catalysts retain their activity trends following Ni amounts in the sandwich layer and size of the Pd−Ni−Pt NPs. Recent reports show that larger sized particles are more sensitive toward nonprecious metal leaching in acidic conditions, making them unstable and less active over time.[60] Since the particle size here is above the limit proposed, we would expect to see activity changes over time due to this effect. Figure S4c shows the transient current density plot over an extended time frame. An increase in the activity is observed for the Ni-containing catalysts after the initial drop from 0 s, where they rise to reach a plateau before they finally begin to decay. Markovic *et al.* have discussed a similar feature for Pt−Ru alloy surfaces as being due to poisoning and removal of CO adsorbed after an initial period of time by Ru sites, however this feature on the Pd−Ni−Pt catalysts is unexpected given the conformal Pt-coating, unless dealloying is occurring.[58] The reason for this and the variation in activity for reaction in acidic media would become clear upon examination of the catalyst structure after electrochemical experiments.

Re-examination of Pd−Ni−Pt Sandwich Nanoparticles after Electrocatalysis Experiments. We initially assumed that the improved performance of the small Pd−Ni−Pt catalysts and the difference in activity for higher Ni amounts in the sandwich layer were lattice strain-related based on the catalytic trends, XRD peak shifts and tailing, and HRTEM of the catalysts before the reactions; however, this assumes the NP surfaces underwent no changes during the potential cycling in acid and base electrolyte. The catalysts were re-examined in TEM after the electrochemical experiments were carried out to confirm whether or not the layered NP structure remained intact. The images of the highest-performing catalysts (small and large Pd−Ni−Pt NPs with the thickest Ni layer) on the carbon support after CA experiments in acidic FOR and basic MOR are shown in Figure 7. A stark difference is apparent in the NP catalysts after reaction in acidic conditions in Figure 7e−), whereas after reaction in base in Figure 7a−d, the structure resembles that before electrochemistry is carried out. For FOR in perchloric acid and blank scans in sulfuric acid, the core of the Pd−Ni−Pt NPs appears void, despite the Pt coating. The Pd and Ni signals remaining in EDX of the sample indicate the metals are not completely removed, however, and this suggests Pd and Ni sites remain in the frameworks.

Following from the TEM results, the case of MOR in KOH solution where catalyst stability is higher, strain governs reactivity, whereas in acidic FOR and MOR conditions, the NPs restructure so that a combination of strain, ligand, and ensemble effects govern the reactivity trends. Before reaction, we believe the compressive strain on the Pt surface may be highest in the small Pd−Ni−Pt NPs, due to the combined strain effects from Ni sandwich layers and smaller size, followed by the larger NPs with ∼4.1 nm Ni, the NPs with ∼2.5 nm Ni, and the Pd−Pt control NPs. This would explain the enhanced catalytic performance in basic MOR. The higher activity with increasing amounts of Ni and decreasing overall NP size for both FOR and MOR in acidic conditions is more likely a result of a combination of this effect and composition changes from dealloying and restructuring. Notably, the hollow structures observed after cycling in acid resemble recent displays of electrocatalysts with stable porous M−Pt nanosheets and nanoframeworks,[61,62] although formed by a different route. The Pt−Ni nanoframeworks produced by C. Chen, Y. Kang *et al.* were formed from oxidative aging of the particles in solution after the synthesis and still showed considerable

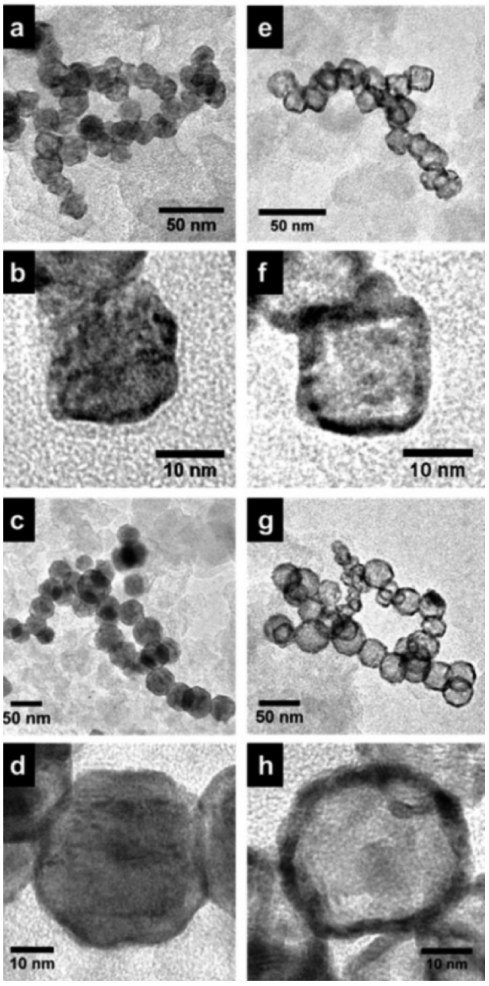

Figure 7. TEM images of cubic Pd−Ni−Pt NPs on the carbon support after the electrochemical experiments in acid and base electrolyte. Images of small Pd−Ni−Pt NPs are given after reaction in basic conditions in (a and b) and acidic conditions in (e and f). (c, d) and (g,h) The large Pd−Ni−Pt NPs after reaction in basic and acidic media, respectively.

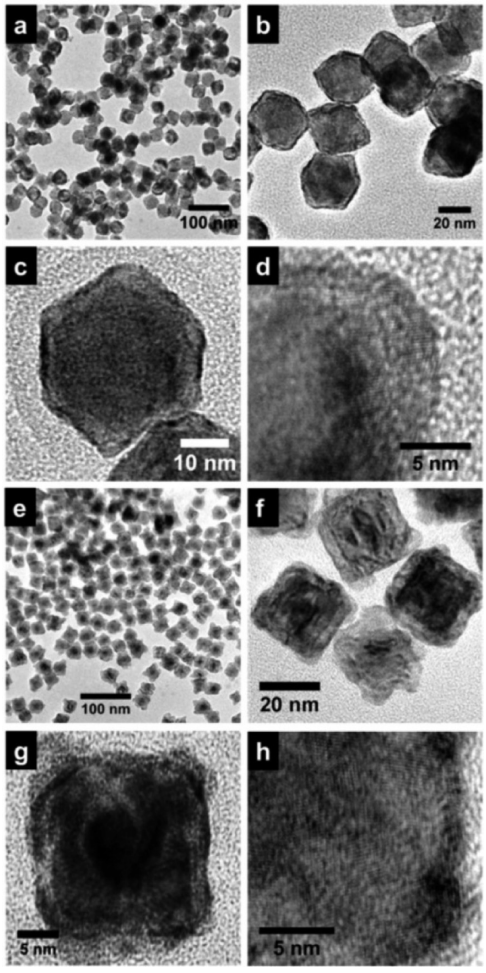

Figure 8. (a−d) TEM and HRTEM images of ~30 nm Pd−Ni−Pt nanooctahedra; (e−h) images of cubic multishelled Au−Pd−Ni-Pt quaternary metal NPs. (c and g) TEM images of single particles are shown where each of the multiple metal phases can be resolved by contrast, and HRTEM images of the respective NPs are given in (d and h).

enhancement and stability for oxygen reduction catalysis. These examples support the finding of increased activity of the catalysts after leaching of Pd and Ni. The postcycling TEM also suggests that even Pd in a core−shell configuration is susceptible to leaching effects from potential cycling in acid, and examination of such Pd-containing electrocatalysts after reaction should not be excluded from future studies.

Synthesis of Quaternary, Multishelled Au−Pd−Ni−Pt Nanoparticles and Pd−Ni−Pt Sandwich Nanooctahedra. Lastly, we demonstrate the synthesis affords differently shaped and more sophisticated layered nanostructures. It was found that the Ni and Pt overgrowth could be replicated on ~30 nm Pd octahedra and on cubic Au−Pd core−shell substrates. This was accomplished by replacing the Pd nanocubes with Pd octahedra or Au−Pd core−shell nanocubes in the growth solution. The resulting NP TEM images are shown in Figure 8. The octahedral ternary metal NPs appear in Figure 8a−d and the cubic quaternary metal NPs appear in Figure 8e−h. The octahedral Pd−Ni−Pt NPs are expected to be the subject of future work as promising candidates for oxygen reduction catalysis (ORR) for fuel cell cathodes. In the high magnification TEM image in Figure 8g, the four metal phases in one of the quaternary cubic NPs can be resolved. A gold cuboctahedral seed is established in the core as the darkest contrast, with a slightly brighter, distinct cubic Pd shell encasing it. As before with the cubic ternary metal NPs, a thin layer of lighter contrast Ni phase surrounds the Au−Pd cube followed by a thin, dark band of Pt at the surface. This shows our method could be used to create NPs with as many as four different and distinguishable metal layers while holding the particle size at or below ~20 nm. The shaped multishelled metal NPs displayed in this work are rare in the literature, to our knowledge, though there is an excellent example of hollow ternary layered noble metal NPs from González *et al.*[63] A recolored TEM image of the Au−Pd−Ni−Pt NP is given in Supporting Information Figure S5 to

more clearly show the four metal phases along with EDX data to confirm the metal composition in the NPs.

CONCLUSION

Shaped Pd–Ni–Pt core-sandwich-shell NPs are synthesized using cubic and octahedral Pd substrates in the aqueous phase at low temperature with cationic surfactant and hydrazine as the reducing agent. It has been demonstrated that the method produces ternary and quaternary multilayered metal nanoparticles comprising Ni with control of shape, size, and Ni layer thickness. Importantly, the one-pot, layer-by-layer overgrowth strategy allows for "trapping" of the pristine, metallic Ni layer before surface oxidation occurs. The novel NP structures are characterized and served as a platform to study the activity of the catalysts in the electrocatalytic oxidation of methanol and formic acid. Their stability is also assessed *via* chronoamperometry. The improved performance of the Pd–Ni–Pt particles over the Pd–Pt control results from increased compressive strain on the Pt surface. It was found that the smaller sized particles and larger Ni sandwich layers are more active and stable over a longer period of time, suggesting a potentially effective catalyst design in future work. Further investigations are aimed at a systematic study of the impact of different shapes and different Ni and Pt layer thicknesses on electrocatalysis by the multishelled structures; in particular, the tuning of the Ni and Pt shell thickness of octahedral Pd–Ni–Pt NPs to obtain a better-performing ORR catalyst.

METHODS

Chemicals. Nickel(II)chloride hexahydrate ($NiCl_2 \cdot 6H_2O$), potassium tetrachloroplatinate(II) (K_2PtCl_4), L-ascorbic acid (AA, 99%), potassium hydroxide (KOH), and formic acid (HCOOH, 88%) were obtained from Sigma-Aldrich. Hydrazine monohydrate ($N_2H_4 \cdot H_2O$, 98%) and perchloric acid ($HClO_4$, 70%) were obtained from Alfa Aesar. Cetyltrimethylammonium bromide (CTAB, 99%) was obtained from Calbiochem, and sulfuric acid (H_2SO_4, 95%) was obtained from BDH. Methanol (CH_3OH, 99.8%) was obtained from Acros. Deionized water (DI water, 18.2 MΩ) was utilized in all experiments. Nitrogen gas was obtained from Airgas.

Synthesis of Cubic Pd–Ni–Pt Nanoparticles. Cubic Pd substrates of two sizes (~10 and ~30 nm) were first prepared according to references.[27−29] A solution containing 0.05 g of CTAB in 10 mL of DI water was then prepared by sonication in a 20 mL glass vial. Then, 500 μL of the concentrated Pd nanocube solution (containing Pd cubes from eight reactions, redispersed in 10 mL DI water) was added to the vial, which was gently mixed. Next, 100 μL of 0.01 M $NiCl_2$ was added as the source of Ni^{2+} ions followed by 500 μL of 1.0 M hydrazine solution. Finally, the vial was vortexed, capped, and left unstirred for ~2 h in a water bath set to 50 °C. A color change from brown to gray/black occurred indicating the completed overgrowth. At this time, the vial was removed from the bath, briefly sonicated, uncapped, and 50 μL of 0.01 M K_2PtCl_4 was injected followed by capping, gentle mixing, and brief sonication (1–2 s). The solution was then returned to the water bath for ~1 h at the same temperature and the Pd–Ni–Pt core-sandwich-shell NPs were then collected *via* centrifugation at 4000 rpm. The thickness of Ni and Pt could be changed by varying the amount of precursor in the growth solution; however, larger amounts of Ni precursor (in excess of 200 μL) led to precipitation of the particles before Pt ions were added.

Synthesis of Cubic Pd–Pt Nanoparticles. The Pd–Pt core–shell NPs were synthesized under the same conditions as the Pd–Ni–Pt NPs, excepting that Ni ions were not added, and ascorbic acid was used as the reducing agent, instead of hydrazine. Briefly, 250 μL of 0.01 M K_2PtCl_4 was added to an aqueous CTAB solution containing the ~30 nm Pd nanocubes in a 20 mL scintillation vial. The solution was mixed and heated for ~5 min at 50 °C with stirring, after which 200 μL of 0.04 M ascorbic acid was added. The vial was left open, heating at this temperature with stirring for ~2 h. Finally, the vial was removed from heat and the NPs were collected by centrifugation at 5000 rpm for 10 min.

Synthesis of Cubic Au–Pd–Ni-Pt Nanoparticles. The ~10–12 nm cubic Au–Pd core–shell substrates were synthesized according to a procedure from a ref 27 with modifications; mainly, the overgrowth of Pd on Au cuboctahedral seeds was scaled up. Typically, the reagent amounts were increased by a factor of 10 without a loss in quality of the cubic shape. A 250 mL beaker was used instead of a scintillation vial, and this was sealed with a paraffin film for the duration of the reaction. These were then collected as before for use in the Ni–Pt overgrowth.

Synthesis of Octahedral Pd–Ni–Pt Nanoparticles. The ~30 nm Pd–Ni–Pt octahedra were synthesized under the same conditions as the cubic Pd–Ni–Pt NPs, except that 500 μL of concentrated ~30 nm Pd octahedra solution, prepared according to ref 27, was used in place of the ~30 nm nanocubes.

Characterization. For analysis by transmission electron microscopy (TEM), energy dispersive X-ray spectroscopy (EDX) and powder X-ray diffraction (XRD), samples were cleaned by three cycles of centrifugation, removal of the supernatant, and redispersion in DI water. After this, the final collection of particles was dispersed in ~50–100 μL of DI water. For TEM characterization, 2 μL of the concentrated nanoparticle solution was placed directly on a carbon-coated copper grid and allowed to dry. Alternatively, particles could be dropcast in 20 μL aliquots on the copper grids. The instrument used was a JEOL JEM2010F accompanied by an EDX attachment operated at 200 kV. For XRD, particles were concentrated in 20 μL of solution which was placed as a droplet on a thin glass slide and allowed to dry. A Bruker AXS D2 Phaser diffractometer was used for the XRD characterization.

STEM/EDX. High-resolution STEM and EDX mapping experiments were performed on a FEI Probe Cs corrected Titan operating at 200 kV. The high angle annular dark field (HAADF) images were obtained using a Fischione HAADF detector, and the EDX maps were acquired with ChemiSTEM technology with four windowless SDD detectors. The instrument incorporates the condenser spherical aberration corrector and X-FEG with probe current 0.4 nA in 0.31 nm spot and can achieve the resolution 0.08 nm as well as efficient X-ray collection rate.

Electrochemical Measurements. The Pd–Ni–Pt NP catalysts were loaded directly onto a glassy carbon working electrode (CH Instruments) without the use of a support for cyclic voltammetry. Typically, 2 μL droplets were placed on the electrode surface and allowed to dry. The cyclic voltammetry (CV) and chronoamperometry (CA) was done using a BioLogic VSP potentiostat in a three electrode system. A saturated calomel electrode was used as the reference electrode and a platinum wire as the counter electrode (both also obtained from CH Instruments). The acidic blank scans were carried out in 0.5 M sulfuric acid solution purged with nitrogen and cycled from −0.2 to 1.0 V at a scan rate of 100 mV/s. These cycles were typically continued until stable voltammagrams were obtained

(~30−50 cycles). The alkaline blank scans were carried out in 0.1 M potassium hydroxide solution purged with nitrogen and cycled from −0.8 to 0.4 V at a scan rate of 100 mV/s. Approximately 20−30 cycles were run in this way until stable curves were reached. The electrochemically active surface area was determined by integration of the total charge collected from the hydrogen desorption peak and dividing this value by the charge per area required to remove the layer of hydrogen from the Pt surface (210 $\mu C/cm^2$).

The alkaline electrooxdiation of methanol was done in 0.05 M methanol and 0.1 M KOH solution. The scan rate was 100 mV/s and the cycles were run from −0.8 to 0.4 V. The highest initial activity usually occurred within the first 20 cycles and the reaction was stopped. The electrooxidation of formic acid was done in a solution which was 0.5 M in HCOOH and 0.5 M in $HClO_4$. The scan rate was 100 mV/s and the range was −0.2 to 1.2 V. The highest initial activity usually occurred within the first ~20 cycles and the reaction was stopped. Methanol oxidation reactions in acid were carried out in a solution, which was 0.5 M in CH_3OH and 0.5 M in H_2SO_4. The scan rate was 100 mV/s and the range was 0−1.0 V. The highest initial activity was usually obtained within ~20 cycles and the experiment was stopped.

The CA curves for MOR in base and for FOR were obtained under identical conditions as previously described, except that the voltage was held constant at −0.1 and 0.4 V, respectively, and the current was measured over time. These potentials were chosen because of good overlap with the potential where peak current was obtained for each of the catalysts. The NP catalysts were put onto a Vulcan carbon support for the CA studies. A 20% by weight catalyst/carbon loading was used. For example, ~2 mg of the Vulcan XC-72 was added directly to a solution containing ~0.5 mg of dispersed NPs. This was then briefly sonicated, and the freshly prepared catalyst/carbon dispersion was then loaded onto the working electrode in 2−3 μL droplets and allowed to dry for the transient current density experiments. The catalysts were cycled in the blank solution and until initial activity was reached prior to the CA run. A blank scan was carried out just prior to the CA experiment in order to obtain a more accurate surface area determination for normalization of the catalytic activity.

Conflict of Interest: The authors declare no competing financial interest.

Acknowledgment. Thanks to Boston College for funding the research. D. Jalalpoor thanks the Evangelisches Studienwerk e.V. for funding of the exchange. Thanks to C. Brodsky for valuable discussions on electrochemical measurements. We thank the Wilson group (BC Physics Dept.) for the use of their diffractometer. Thanks also to G. McMahon for assistance with TEM and EDX.

Supporting Information Available: Additional experiments and discussion which includes TEM images of Pd−Ni NPs without the Pt overgrowth, TEM of Pd nanocube substrates before the overgrowth, EDX measurements of the quaternary metal NPs with a recolored TEM image, electrochemical blank scans for the four catalysts, additional CA plots, and a more detailed synthesis scheme for making the cubic Pd−Ni−Pt NPs. This material is available free of charge *via* the Internet at http://pubs.acs.org.

REFERENCES AND NOTES

1. Mayrhofer, K. J. J.; Arenz, M. Fuel Cells: Log on for New Catalysts. *Nat. Chem.* **2009**, *1*, 518–519.
2. Debe, M. K. Electrocatalyst Approaches and Challenges for Automotive Fuel Cells. *Nature.* **2012**, *486*, 43–51.
3. Stephens, I. E. L.; Bondarenko, A. S.; Gronbjerg, U.; Rossmeisl, J.; Chorkendorff, I. Understanding the Electrocatalysis of Oxygen Reduction on Platinum and its Alloys. *Energy Environ. Sci.* **2012**, *5*, 6744–6762.
4. Norskov, J. K.; Bligaard, T.; Rossmeisl, J.; Christensen, C. H. Towards the Computational Design of Solid Catalysts. *Nat. Chem.* **2009**, *1*, 37–46.
5. Long, N. V.; Thi, C. M.; Yong, Y.; Nogami, M.; Ohtaki, M. Platinum and Palladium Nano-Structured Catalysts for Polymer Electrolyte Fuel Cells and Direct Methanol Fuel Cells. *J. Nanosci. Nanotechnol.* **2013**, *13*, 4799–4824.
6. Singh, A. K.; Xu, Q. Synergistic Catalysis over Bimetallic Alloy Nanoparticles. *ChemCatChem* **2013**, *5*, 652–676.
7. Guo, S.; Zhang, S.; Sun, S. Tuning Nanoparticle Catalysis for the Oxygen Reduction Reaction. *Angew. Chem., Int. Ed.* **2013**, *52*, 8526–8544.
8. Bandarenka, A. S.; Koper, M. T. M. Structural and Electronic Effects in Heterogeneous Electrocatalysis: Toward a Rational Design of Electrocatalysts. *J. Catal.* **2013**, *308*, 11–24.
9. Wu, B. H.; Zheng, N. F. Surface and Interface Control of Noble Metal Nanocrystals for Catalytic and Electrocatalytic applications. *Nano Today* **2013**, *8*, 168–197.
10. Oezaslan, M.; Hasché, F.; Strasser, P. Pt-Based Core−Shell Catalyst Architectures for Oxygen Fuel Cell Electrodes. *J. Phys. Chem. Lett.* **2013**, *4*, 3273–3291.
11. Kaya, S.; Friebel, D.; Ogasawara, H.; Anniyev, T.; Nilsson, A. Electronic Structure Effects in Catalysis Probed by X-ray and Electron Spectroscopy. *J. Electron Spectrosc. Relat. Phenom.* **2013**, *190* (Part A), 113–124.
12. Zhang, X.; Lu, G. Computational Design of Core/Shell Nanoparticles for Oxygen Reduction Reactions. *J. Phys. Chem. Lett.* **2013**, *5*, 292–297.
13. Wang, G.; Van Hove, M. A.; Ross, P. N.; Baskes, M. I. Monte Carlo Simulations of Segregation in Pt-Ni Catalyst Nanoparticles. *J. Chem. Phys.* **2005**, *122*, 024706.
14. Menning, C. A.; Hwu, H. H.; Chen, J. G. Experimental and Theoretical Investigation of the Stability of Pt−3d−Pt(111) Bimetallic Surfaces under Oxygen Environment. *J. Phys. Chem. B* **2006**, *110*, 15471–15477.
15. Wang, C.; Chi, M.; Li, D.; Strmcnik, D.; van der Vliet, D.; Wang, G.; Komanicky, V.; Chang, K.-C.; Paulikas, A. P.; Tripkovic, D.; *et al.* Design and Synthesis of Bimetallic Electrocatalyst with Multilayered Pt-Skin Surfaces. *J. Am. Chem. Soc.* **2011**, *133*, 14396–14403.
16. Porosoff, M. D.; Yu, W.; Chen, J. G. Challenges and Opportunities in Correlating Bimetallic Model Surfaces and Supported Catalysts. *J. Catal.* **2013**, *308*, 2–10.
17. Cui, C.; Gan, L.; Heggen, M.; Rudi, S.; Strasser, P. Compositional Segregation in Shaped Pt Alloy Nanoparticles and Their Structural Behaviour During Electrocatalysis. *Nat. Mater.* **2013**, *12*, 765–771.
18. Strasser, P.; Koh, S.; Anniyev, T.; Greeley, J.; More, K.; Yu, C.; Liu, Z.; Kaya, S.; Nordlund, D.; Ogasawara, H.; *et al.* Lattice-Strain Control of the Activity in Dealloyed Core−Shell Fuel Cell Catalysts. *Nat. Chem.* **2010**, *2*, 454–460.
19. Cui, C.; Gan, L.; Li, H.-H.; Yu, S.-H.; Heggen, M.; Strasser, P. Octahedral PtNi Nanoparticle Catalysts: Exceptional Oxygen Reduction Activity by Tuning the Alloy Particle Surface Composition. *Nano Lett.* **2012**, *12*, 5885–5889.
20. Choi, S.-I.; Xie, S.; Shao, M.; Odell, J. H.; Lu, N.; Peng, H.-C.; Protsailo, L.; Guerrero, S.; Park, J.; Xia, X.; *et al.* Synthesis and Characterization of 9 nm Pt−Ni Octahedra with a Record High Activity of 3.3 A/mgPt for the Oxygen Reduction Reaction. *Nano Lett.* **2013**, *13*, 3420–3425.
21. Wu, J.; Gross, A.; Yang, H. Shape and Composition-Controlled Platinum Alloy Nanocrystals Using Carbon Monoxide as Reducing Agent. *Nano Lett.* **2011**, *11*, 798–802.
22. Porter, N. S.; Wu, H.; Quan, Z.; Fang, J. Shape-Control and Electrocatalytic Activity-Enhancement of Pt-Based Bimetallic Nanocrystals. *Acc. Chem. Res.* **2013**, *46*, 1867–1877.
23. Wu, Y.; Cai, S.; Wang, D.; He, W.; Li, Y. Syntheses of Water-Soluble Octahedral, Truncated Octahedral, and Cubic Pt−Ni Nanocrystals and Their Structure−Activity Study in Model Hydrogenation Reactions. *J. Am. Chem. Soc.* **2012**, *134*, 8975–8981.
24. Jin, M.; Zhang, H.; Wang, J.; Zhong, X.; Lu, N.; Li, Z.; Xie, Z.; Kim, M. J.; Xia, Y. Copper Can Still Be Epitaxially Deposited on Palladium Nanocrystals To Generate Core−Shell Nanocubes Despite Their Large Lattice Mismatch. *ACS Nano* **2012**, *6*, 2566–2573.
25. Ping, H.; Chen, Y.; Guo, H.; Wang, Z.; Zeng, D.; Wang, L.; Peng, D.-L. A Facile Solution Approach for the Preparation

of Ag@Ni Core−Shell Nanocubes. *Mater. Lett.* **2014**, *116*, 239–242.
26. Sau, T. K.; Murphy, C. J. Room Temperature, High-yield Synthesis of Multiple Shapes of Gold Nanoparticles in Aqueous Solution. *J. Am. Chem. Soc.* **2004**, *126*, 8648–8649.
27. Kuo, C.-H.; Lamontagne, L. K.; Brodsky, C. N.; Chou, L.-Y.; Zhuang, J.; Sneed, B. T.; Sheehan, M. K.; Tsung, C.-K. The Effect of Lattice Strain on the Catalytic Properties of Pd Nanocrystals. *ChemSusChem.* **2013**, *6*, 1993–2000.
28. Sneed, B. T.; Kuo, C.-H.; Brodsky, C. N.; Tsung, C.-K. Iodide-Mediated Control of Rhodium Epitaxial Growth on Well-Defined Noble Metal Nanocrystals: Synthesis, Characterization, and Structure-Dependent Catalytic Properties. *J. Am. Chem. Soc.* **2012**, *134*, 18417–18426.
29. Sneed, B. T.; Brodsky, C. N.; Kuo, C.-H.; Lamontagne, L. K.; Jiang, Y.; Wang, Y.; Tao, F.; Huang, W.; Tsung, C.-K. Nanoscale-Phase-Separated Pd−Rh Boxes Synthesized *via* Metal Migration: An Archetype for Studying Lattice Strain and Composition Effects in Electrocatalysis. *J. Am. Chem. Soc.* **2013**, *135*, 14691–14700.
30. Habas, S. E.; Lee, H.; Radmilovic, V.; Somorjai, G. A.; Yang, P. Shaping Binary Metal Nanocrystals Through Epitaxial Seeded Growth. *Nat. Mater.* **2007**, *6*, 692–697.
31. DeSantis, C. J.; Sue, A. C.; Bower, M. M.; Skrabalak, S. E. Seed-Mediated Co-reduction: A Versatile Route to Architecturally Controlled Bimetallic Nanostructures. *ACS Nano* **2012**, *6*, 2617–2628.
32. Kuo, C. H.; Hua, T. E.; Huang, M. H. Au Nanocrystal-Directed Growth of Au-Cu_2O Core-Shell Heterostructures with Precise Morphological Control. *J. Am. Chem. Soc.* **2009**, *131*, 17871–17878.
33. Wang, J. X.; Inada, H.; Wu, L.; Zhu, Y.; Choi, Y.; Liu, P.; Zhou, W.-P.; Adzic, R. R. Oxygen Reduction on Well-Defined Core−Shell Nanocatalysts: Particle Size, Facet, and Pt Shell Thickness Effects. *J. Am. Chem. Soc.* **2009**, *131*, 17298–17302.
34. Hwang, S. J.; Kim, S.-K.; Lee, J.-G.; Lee, S.-C.; Jang, J. H.; Kim, P.; Lim, T.-H.; Sung, Y.-E.; Yoo, S. J. Role of Electronic Perturbation in Stability and Activity of Pt-Based Alloy Nanocatalysts for Oxygen Reduction. *J. Am. Chem. Soc.* **2012**, *134*, 19508–19511.
35. Xin, H.; Linic, S. Communications: Exceptions to the d-band Model of Chemisorption on Metal Surfaces: The Dominant Role of Repulsion Between Adsorbate States and Metal d-states. *J. Chem. Phys.* **2010**, *132*, 221101.
36. Yu, T. H.; Hofmann, T.; Sha, Y.; Merinov, B. V.; Myers, D. J.; Heske, C.; Goddard, W. A. Finding Correlations of the Oxygen Reduction Reaction Activity of Transition Metal Catalysts with Parameters Obtained from Quantum Mechanics. *J. Phys. Chem. C* **2013**, *117*, 26598–26607.
37. Koper, M. T. M. Structure Sensitivity and Nanoscale Effects in Electrocatalysis. *Nanoscale* **2011**, *3*, 2054–2073.
38. Grzelczak, M.; Pérez-Juste, J.; Rodríguez-González, B.; Spasova, M.; Barsukov, I.; Farle, M.; Liz-Marzán, L. M. Pt-Catalyzed Growth of Ni Nanoparticles in Aqueous CTAB Solution. *Chem. Mater.* **2008**, *20*, 5399–5405.
39. Sanles-Sobrido, M.; Banobre-Lopez, M.; Salgueirino, V.; Correa-Duarte, M. A.; Rodriguez-Gonzalez, B.; Rivas, J.; Liz-Marzan, L. M. Tailoring the Magnetic Properties of Nickel Nanoshells Through Controlled Chemical Growth. *J. Mater. Chem.* **2010**, *20*, 7360–7365.
40. Grzelczak, M.; Rodríguez-González, B.; Pérez-Juste, J.; Liz-Marzán, L. M. Quasi-Epitaxial Growth of Ni Nanoshells on Au Nanorods. *Adv. Mater.* **2007**, *19*, 2262–2266.
41. Sánchez-Iglesias, A.; Grzelczak, M.; Rodríguez-González, B.; Guardia-Girós, P.; Pastoriza-Santos, I.; Pérez-Juste, J.; Prato, M.; Liz-Marzán, L. M. Synthesis of Multifunctional Composite Microgels *via in Situ* Ni Growth on pNIPAM-Coated Au Nanoparticles. *ACS Nano* **2009**, *3*, 3184–3190.
42. Wu, Z. G.; Munoz, M.; Montero, O. The Synthesvsis of Nickel Nanoparticles by Hydrazine Reduction. *Adv. Powder Technol.* **2010**, *21*, 165–168.
43. Sarkar, S.; Sinha, A. K.; Pradhan, M.; Basu, M.; Negishi, Y.; Pal, T. Redox Transmetalation of Prickly Nickel Nanowires for Morphology Controlled Hierarchical Synthesis of Nickel/Gold Nanostructures for Enhanced Catalytic Activity and SERS Responsive Functional Material. *J. Phys. Chem. C* **2010**, *115*, 1659–1673.
44. Senapati, S.; Srivastava, S. K.; Singh, S. B.; Biswas, K. Capping Agent Assisted and Ag-Catalyzed Growth of Ni Nanoflowers. *Cryst. Growth Des.* **2010**, *10*, 4068–4075.
45. Nelson, N. C.; Ruberu, T. P. A.; Reichert, M. D.; Vela, J. Templated Synthesis and Chemical Behavior of Nickel Nanoparticles within High Aspect Ratio Silica Capsules. *J. Phys. Chem. C* **2013**, *117*, 25826–25836.
46. Jana, S.; Chang, J. W.; Rioux, R. M. Synthesis and Modeling of Hollow Intermetallic Ni−Zn Nanoparticles Formed by the Kirkendall Effect. *Nano Lett.* **2013**, *13*, 3618–3625.
47. Zhang, W.-B.; Chen, C.; Zhang, S.-Y. Equilibrium Crystal Shape of Ni from First Principles. *J. Phys. Chem. C* **2013**, *117*, 21274–21280.
48. Ming, T.; Feng, W.; Tang, Q.; Wang, F.; Sun, L. D.; Wang, J. F.; Yan, C. H. Growth of Tetrahexahedral Gold Nanocrystals with High-index Facets. *J. Am. Chem. Soc.* **2009**, *131*, 16350−+.
49. Wu, H. L.; Kuo, C. H.; Huang, M. H. Seed-Mediated Synthesis of Gold Nanocrystals with Systematic Shape Evolution from Cubic to Trisoctahedral and Rhombic Dodecahedral Structures. *Langmuir* **2010**, *26*, 12307–12313.
50. Kuo, C.-H.; Tang, Y.; Chou, L.-Y.; Sneed, B. T.; Brodsky, C. N.; Zhao, Z.; Tsung, C.-K. Yolk−Shell Nanocrystal@ZIF-8 Nanostructures for Gas-Phase Heterogeneous Catalysis with Selectivity Control. *J. Am. Chem. Soc.* **2012**, *134*, 14345–14348.
51. Zhang, B.; Wu, J.; Li, X.; Liu, H.; Yadian, B.; Ramanujan, R. V.; Zhou, K.; Wu, R.; Hao, S.; Huang, Y. Passivation of Nickel Nanoneedles in Aqueous Solutions. *J. Phys. Chem. C* **2014**, *118*, 9073–9077.
52. Lim, B.; Jiang, M.; Camargo, P. H. C.; Cho, E. C.; Tao, J.; Lu, X.; Zhu, Y.; Xia, Y. Pd-Pt Bimetallic Nanodendrites with High Activity for Oxygen Reduction. *Science* **2009**, *324*, 1302–1305.
53. Liu, X.-J.; Cui, C.-H.; Gong, M.; Li, H.-H.; Xue, Y.; Fan, F.-J.; Yu, S.-H. Pt-Ni Alloyed Nanocrystals with Controlled Architectures for Enhanced Methanol Oxidation. *Chem. Commun.* **2013**, *49*, 8704–8706.
54. Kang, Y.; Pyo, J. B.; Ye, X.; Gordon, T. R.; Murray, C. B. Synthesis, Shape Control, and Methanol Electro-oxidation Properties of Pt−Zn Alloy and Pt_3Zn Intermetallic Nanocrystals. *ACS Nano* **2012**, *6*, 5642–5647.
55. Deivaraj, T. C.; Chen, W.; Lee, J. Y. Preparation of PtNi Nanoparticles for the Electrocatalytic Oxidation of Methanol. *J. Mater. Chem.* **2003**, *13*, 2555–2560.
56. Wang, L.; Liu, P.; Guan, P.; Yang, M.; Sun, J.; Cheng, Y.; Hirata, A.; Zhang, Z.; Ma, E.; Chen, M.; *et al. In Situ* Atomic-Scale Observation of Continuous and Reversible Lattice Deformation Beyond the Elastic Limit. *Nat. Commun.* **2013**, *4*, 1–7.
57. Abdel Rahim, M. A.; Hassan, H. B.; Abdel Hameed, R. M. Graphite Electrodes Modified with Platinum-Nickel Nano-Particles for Methanol Oxidation. *Fuel Cells* **2007**, *7*, 298–305.
58. Tripković, A. V.; Popović, K. D.; Grgur, B. N.; Blizanac, B.; Ross, P. N.; Marković, N. M. Methanol Electrooxidation on Supported Pt and PtRu Catalysts in Acid and Alkaline Solutions. *Electrochim. Acta* **2002**, *47*, 3707–3714.
59. Prabhuram, J.; Manoharan, R. Investigation of Methanol Oxidation on Unsupported Platinum Electrodes in Strong Alkali and Strong Acid. *J. Power Sources* **1998**, *74*, 54–61.
60. Gan, L.; Heggen, M.; O'Malley, R.; Theobald, B.; Strasser, P. Understanding and Controlling Nanoporosity Formation for Improving the Stability of Bimetallic Fuel Cell Catalysts. *Nano Lett.* **2013**, *13*, 1131–1138.
61. Jia, Y.; Jiang, Y.; Zhang, J.; Zhang, L.; Chen, Q.; Xie, Z.; Zheng, L. Unique Excavated Rhombic Dodecahedral PtCu3 Alloy Nanocrystals Constructed with Ultrathin Nanosheets of High-Energy {110} Facets. *J. Am. Chem. Soc.* **2014**, *136*, 3748–3751.

62. Chen, C.; Kang, Y.; Huo, Z.; Zhu, Z.; Huang, W.; Xin, H. L.; Snyder, J. D.; Li, D.; Herron, J. A.; Mavrikakis, M.; *et al.* Highly Crystalline Multimetallic Nanoframes with Three-Dimensional Electrocatalytic Surfaces. *Science* **2014**, *343*, 1339–1343.
63. González, E.; Arbiol, J.; Puntes, V. F. Carving at the Nanoscale: Sequential Galvanic Exchange and Kirkendall Growth at Room Temperature. *Science* **2011**, *334*, 1377–1380.